minerals

MDPI

Article

Ultrasonic and Microstructural Evaluation of Sulphide-Rich Tailings Cemented Paste Backfill Properties Containing Alkali-Activated Slag: Effect of Slag Fineness

Ercument Koc [1] and Ferdi Cihangir [2,*]

[1] Department of Metallurgical and Materials Engineering, Ataturk University, 25010 Erzurum, Turkey; ercument.koc@atauni.edu.tr
[2] Department of Mining Engineering, Karadeniz Technical University, 61080 Trabzon, Turkey
* Correspondence: cihangir@ktu.edu.tr; Tel.: +90-462-377-4055

Abstract: Cement paste backfill (CPB) is an effective waste management method allowing the storage of fine process tailings into underground mined-out voids. CPB performance generally depends on the properties of the tailings and the type of binder. In recent years, there has been an increasing trend in the use of alkali-activated slag (AAS) to improve the performance properties of CPB. This study focuses on the ultrasonic and microstructural investigation of the effect of slag fineness on the mechanical, geochemical, and durability properties of sulphide-rich tailings CPB made of AAS (AAS-CPB) over 360 days. In this scope, the AAS-CPB samples were prepared at three different slag fineness values (3100–4650–6300 cm^2/g). According to the findings, the fineness of the slag significantly improved the early-age and long-term strength (~2.3-fold and ~6.6-fold, respectively) of the CPB samples (CPBs). However, a further increase in the slag fineness was observed to impair the CPB microstructure and strength in the long term. Ultrasonic pulse velocity monitoring displayed a very high relation with the strength evolution of the CPBs and is a very reliable method for the durability assessment of the CPBs. Slag fineness around 4600 cm^2/g was found to be sufficient for CPB preparation, and was seen to improve the pore structure evolution of the AAS-CPB. Microstructural studies are in good agreement with the geochemical and durability behaviour of the AAS-CPB at this fineness. Microstructural and ultrasonic findings suggest that, while slag fineness enhances the mechanical and microstructural properties of the AAS-CPB, a further increase in the fineness of the slag has no additional technical advantages.

Keywords: cemented paste backfill; alkali-activated slag; slag fineness; ultrasonic pulse velocity; microstructure; durability

check for updates

Citation: Koc, E.; Cihangir, F. Ultrasonic and Microstructural Evaluation of Sulphide-Rich Tailings Cemented Paste Backfill Properties Containing Alkali-Activated Slag: Effect of Slag Fineness. *Minerals* **2023**, *13*, 1524. https://doi.org/10.3390/min13121524

Academic Editor: Chongchong Qi

Received: 1 November 2023
Revised: 27 November 2023
Accepted: 3 December 2023
Published: 6 December 2023

Copyright: © 2023 by the authors. Licensee MDPI, Basel, Switzerland. This article is an open access article distributed under the terms and conditions of the Creative Commons Attribution (CC BY) license (https://creativecommons.org/licenses/by/4.0/).

1. Introduction

The development and growth of global economies and the investments in technological studies increase the need for underground raw materials day by day. The increasing need for raw materials entails deeper open-pit mining or underground mining operations. In most cases, extracted ores from the Earth's crust necessitate fine grinding and chemical treatments to gain such raw materials/precious metals, etc. As a result, large amounts of mineral processing tailings are produced which may contain environmentally hazardous compounds [1,2].

Environmentally friendly management of these kinds of tailings/wastes is of great importance. Such materials are mostly stored in tailings dams or placed into underground mining voids as cemented paste backfill (CPB). Tailings dams require large areas and constant maintenance, and carry high risks of collapse. On the other hand, the use of CPB technology has been increasing and has become widespread all over the world in the last 40 years, especially in recent years, for the management of these tailings [2–4].

CPB is widely used as a combination of cut-and-fill underground mining methods. It provides many environmental and technical advantages, such as safe working conditions, a high mining cycle, increased ore gain rate and mine life, decrease in the mining cost, etc. [5–9].

CPB is a successfully designed engineering cemented material prepared using fine-processing tailings, water, and cement agents. The performance properties of CPB are very significant during its service life. Strength, durability, and consistency are among the most important properties of CPB. Therefore, the characterisation of each component is very important. Up to today, the binder types and dosages [10,11], physical, mineralogical, and chemical properties [12–14], microstructural, workability, and rheological properties [15–18], and the durability properties of CPB [11,19] have been extensively studied.

The interaction of the binder agent and tailings is very important for CPB performance [20]. Therefore, each tailing entails a special design in the case of the use as CPB material for the desired strength, durability, and consistency. In most cases, CPB has a 30%–50% porosity and 15%–30% moisture as a result of the tailings characteristics. Based on the strength requirements, in general, a 5–10 wt.% binder is used. Additionally, tailings can contain high amounts of sulphidic minerals, such as pyrite. Due to the highly porous structure and high water-retention capacity of CPB in its body for very long periods, pyrite minerals oxidize and generate acid and sulphate products.

Ordinary Portland cement is the most common binder used in CPB applications. However, it is vulnerable to acid and sulphate effects due to its intrinsic properties, such as high CaO and C_3A contents [21,22]. Therefore, there have been extensive studies to overcome this problem and produce a durable CPB [21,23]. In practice, the durability of CPB is followed by unconfined strength tests. Additionally, geochemical and microstructural properties are the other main factors considered for durability assessments. Recently, there has been an increasing interest in the use of alkali-activated slag cement (AAS) for CPB preparation to increase the quality and microstructural properties. In this scope, the slag and activator type [11,21], the tailings type and activator design [19], and the strength, workability, and rheological properties [17,24–26] were studied. Among these, Cihangir and his team investigated the durability of CPB prepared using AAS in the long term. However, the effect of the slag fineness on the mechanical, microstructural, and durability properties of sulphide-rich tailings CPB produced with alkali-activated slag was not investigated in the long term (360 days).

Slag was generally ground above a Blaine value of 3500 cm^2/g to increase the reactivity as well as the gain of strength at early ages [27]. There are numerous studies where the Blaine fineness of slags used to produce alkali-activated slag concretes was in the range of 3300–9000 cm^2/g [28]. On the other hand, the Blaine fineness of the slag varied between 3950 and 6295 cm^2/g in the CPB studies [19,21,25,29–32]. Provis and van Deventer [33] reported that the optimum Blaine fineness of the blast-furnace slag may vary between 4000 and 5000 cm^2/g for a proper strength-gain rate. As can be seen, the slag fineness can vary significantly from study to study. Therefore, the focus of this study is to investigate the effect of the slag fineness (considering the above Blaine fineness interval) on the strength-development rate on the early-age and long-term durability of CPB utilizing the microstructural properties, in detail.

On the other hand, the ultrasonic P-wave velocity (ultrasonic pulse velocity: UPV) test was used recently for the prediction of the UCS of CPB. Physical, mechanical, and geotechnical properties can be determined via the UPV test [34,35]. Additionally, the UPV test is an efficient and non-destructive method that is very sensitive to the bond strength, the compactness of the materials, weathering properties, heterogeneity, structural defects such as cracks, etc., indicating the quality of solid materials [35–37]. UPV is used for the assessment of the durability of concrete materials, taking into account the defects, such as voids and cracks. Microcracks were found to soften the material and lower the stiffness, resulting in the loss of the UPV [38–42]. Additionally, the increase in the volume of the porosity, the bond-strength loss between mineral grains, minerals transformations, etc., due to the weathering caused a loose microstructure and stiffness loss, which resulted in

a lower UPV and mechanical strength [43,44]. Therefore, UPV provides quality control solutions for material classifications [45].

As for CPB, previous studies investigated only the short-term relations between the UCS and UPV of the CPBs up to 7 days [46], 14 days [47], 28 days [48–50], 56 days [26,51–54], and 90 days [26,55,56] of the curing periods. However, no study was carried out for the durability assessment of CPB via UPV in the long term together with the detailed geochemical and microstructural properties of CPB.

Therefore, this is the first study aiming to investigate the effect of the slag fineness and its use as an alkali-activated binder on the mechanical, geochemical, microstructural, and durability properties of CPB. Since UPV is a very sensitive and strong tool for the determination of structural defects, it was also first used for the durability assessment of CPB produced with AAS using slags at different fineness values in the long term.

2. Materials Characterisation and Experimental Studies

2.1. Characterisation of Tailings and Binders

Sulphide-rich tailings for this study were obtained from a copper–zinc plant located in the northwest of Turkey. Tailings were taken from the disc filter outlets in the paste backfill plant and brought to the laboratory. After the homogenization, the particle size distribution (PSD) of the tailings was measured under the laser diffraction method with a Malvern Mastersizer Hydro 2000 MU (Figure 1a). Water was used as a dispersing medium, and ultrasound was also utilized to better disperse the particles. Considering C_u (the coefficient of uniformity) and C_c (the coefficient of curvature) values (Table 1), the tailings material had a well-distributed particle size [18]. It is a medium-sized material with a fine particle content of about 48.85%, under 20 microns [57]. The fineness of the tailings was determined according to TS EN 196-6 [58] in a cement plant located in Trabzon, Turkey. Specific gravity was determined in accordance with the ISRM [59].

Table 1. Chemical, physical, and mineralogical properties of the tailings.

Chemical Composition (%)	Value	Physical Properties	Value	Mineralogical Content (%)	Value
SiO_2	15.24	Specific gravity	3.95	Quartz	15.4
Al_2O_3	3.69	Specific surface (cm^2/g)	3066	Pyrite	56.3
Fe_2O_3	49.19	−20 µm material content (%)	48.85	Clinochlore	4.5
CaO	2.56	D_{10} (µm)	1.84	Kaolinite	3.1
MgO	1.64	D_{30} (µm)	8.44	Calcite	4.5
TiO_2	0.21	D_{50} (µm)	20.97	Amesite	4.1
Cr_2O_3	0.03	D_{60} (µm)	30.37	Siderite	2.0
Na_2O	0.98	D_{90} (µm)	90.37	Dolomite	2.4
K_2O	0.22	C_u	16.51	Acmite	1.1
MnO	0.07	C_c	1.27	Copiapite	1.0
P_2O_5	0.06	Initial pH	8.98	Hematite	2.7
Loss on ignition	23.30	Initial SO_4^{2-} (ppm)	5712	Halloysite	0.8
S^{2-} (Sulphide)	32.33			Gypsum	1.0
Total S	28.89			Others	~1.1

C_u: (D_{60}/D_{10}); C_c: $((D_{30})^2/(D_{10} \times D_{60}))$.

Chemical analysis of the tailings was performed at ACME laboratories in Canada using X-ray fluorescence (XRF) (Table 1). The X-ray diffraction (XRD) analyses were carried out using a Panalytical X'Pert3 Powder model machine equipped with a Pixel 1D detector (Malvern Panalytical, Malvern, UK) in the Karadeniz Technical University Central Research Laboratories (KTU-CRL). The analysis duration was 1 h for each sample, and performed between 5 and 80° under 2θ with a 0.013° step size. The scanning rate was

applied as 1.25° per minute for the reliable determination of the crystalline phases of the materials (Figure 1b). Under these conditions, the Rietveld technique was conducted for the determination of the mineralogical contents (Table 1). As can be seen from Table 1, pyrite was the dominant mineral.

Ordinary Portland cement (OPC: CEM I 42.5R) was obtained from a cement company in Trabzon, Turkey. Ground granulated blast-furnace slag was taken from an iron–steel company located in the northwest of Turkey. Then, the slag was ground in steel ball mill to reach the previously determined specific surface areas (SSA: Blain fineness) of 3100, 4650, and 6300 cm^2/g. The Blaine fineness of the slags was measured at the abovementioned cement plant in accordance with TS EN 196-6 [58]. Chemical, physical, and mineralogical analyses were performed together with the tailings under the same standards/methods at the same laboratories mentioned above. According to the chemical composition, slag had an acidic character with a basicity index (BI) value of 0.96. The BI value was calculated using the formula suggested by Bauné et al. [60]. The pozzolanic activity index test was also performed in the Turkey Cement Manufacturers Research Laboratories located in Ankara, Turkey, in accordance with ASTM C989/989M-22 [61], to evaluate the effect of the fineness on the pozzolanic properties (Table 2). For the particle size distribution of the binders, the wet dispersion method was also used, since the cement particles tend to agglomerate in a dry state. Ethanol was used as a dispersive medium to prevent the dissolution of the cement and slag particles, and ultrasound was also utilised during the PSD measurements. The slag had a glassy phase, with some weak amorphous Ca-containing low peaks (Figure 1b). The PSD and XRD profiles of the materials are given in Figure 1a,b.

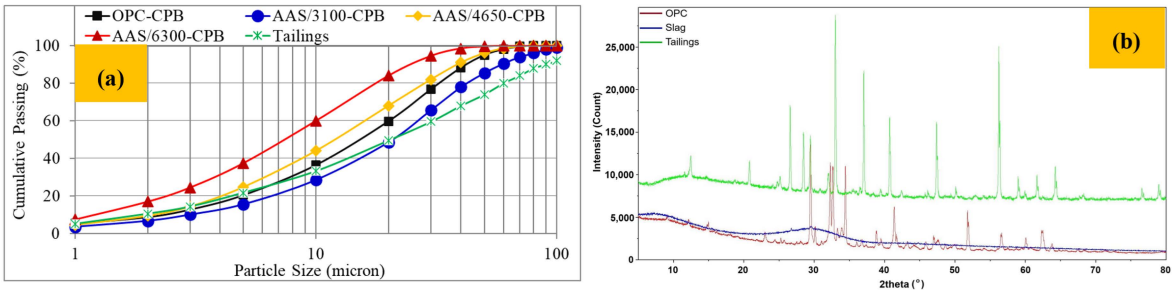

Figure 1. Particle size distributions (**a**) and XRD profiles (**b**) of the materials.

Table 2. Chemical, mineralogical, and physical properties of binders.

Chemical Composition (%)	OPC (%)	Slag (%)	Physical Properties	OPC	Slag 3100	Slag 4650	Slag 6300
SiO_2	19.10	40.24	Specific gravity	3.15	2.90	2.90	2.90
Al_2O_3	5.35	11.68	Specific surface (cm^2/g)	4060	3100	4650	6300
Fe_2O_3	3.45	0.66	+90 µm sieve (%)	-	0.8	-	-
CaO	62.29	36.63	+45 µm sieve (%)	2.64	12.3	3.85	0.62
MgO	0.95	5.90	+32 µm sieve (%)	7.11	24.6	8.33	2.78
TiO_2	0.14	1.00	Mineralogical composition *				
Cr_2O_3	0.007	0.006					
Na_2O	0.41	0.3	C_3S	64.1	-	-	-
K_2O	1.09	1.27	C_2S	26.0	-	-	-
MnO	0.07	1.98	C_3A	3.0	-	-	-
P_2O_5	0.08	0.01	C_4AF	3.7	-	-	-
Loss on ignition	1.53	0.9	Basicity index	-		0.96	
SO_3	6.68	1.71	Pozzolanic index (%; 28 days)	-	67.6	84.7	99.3

*: The mineralogical composition of the cement was determined under the XRD Rietveld technique.

Liquid sodium silicate (LSS: 11.02% Na_2O, 22.1% SiO_2) obtained from Ege Chemicals Ltd. (Istanbul, Turkey) and Merck-brand (Rahway, NJ, USA) granular sodium hydroxide (SH: 99.5%) were used as activators. Taking into account the authors' previous studies, the modulus ratio of the sodium silicate (MS: mass ratio of SiO_2 to Na_2O) was set to 1.0 using SH, while the activator dosage was fixed at 8.0 wt.% of the slag on a dry basis.

2.2. Preparation of the CPBs and Strength Tests

The CPB samples were prepared in four different recipes (Table 3) with ordinary Portland cement (OPC) and alkali-activated slags (AASs) having different specific surface areas (3100 cm^2/g (AAS-3100), 4650 cm^2/g (AAS-4600), and 6300 cm^2/g (AAS-6300)). The binder dosage for the CPB preparation was set to 7 wt.% on a dry basis of the total solids (tailings + binders).

Table 3. CPB design conditions.

Binder Type	Binder Content	Solid Content (%)	Water Content (%)	Water/Binder Ratio	Slump (inch)
AAS-3100	7%	80.31	19.69	3.50	8.6
AAS-4650	7%	80.24	19.76	3.52	8.4
AAS-6300	7%	80.16	19.84	3,54	8.3
OPC	7%	77.97	22.03	4.04	8.4

After mixing, fresh CPB material at an 8.5 ± 0.2-inch slump height (~216 mm), measured according to ASTM C143/C143M-20 [62], was poured into plastic moulds of 54 mm in diameter and 108 mm in height, with a perforated bottom for the drainage of excess water. A total of 96 CPBs were produced for the experimental studies, 72 of which were used for the UPV, UCS, pH, and sulphate tests at 14–28–56–112–224–360 days. After the mouths of the sample moulds were sealed with parafilm, they were placed in two nested separate plastic bags whose mouths were also tied separately. Thus, the contact of the CPB samples with air was inhibited. After that, the CPBs were put into a temperature-controlled curing cabinet with a humidifier at 20 ± 1 °C and %85 ± 1 humidity conditions.

The CPBs were subjected to UCS testing, in accordance with ASTM C39/C39M-21 [63], using a 50 kN servo-controlled compression machine with a loading rate of 0.5 mm per minute. Tests were carried out on 3 CPBs at each curing time, and the average values are presented in the Results. Strength and durability assessments were made considering a 1.0 MPa threshold value in the short and long term, as suggested by Landriault [57].

2.3. The pH and Sulphate Monitoring

The pH and sulphate analyses were conducted on the CPBs after the UCS testing for the evaluation of the acid and sulphate effects on the properties of the CPBs. One of the most important indications of pyrite oxidation generating acid and sulphate products is the pH. Portlandite completely dissolves when the pH drops under 12 [64,65], leaving a porous structure behind [66], and also causing the weakening of the bond strength of C-S-H due to the decalcification [67]. When the pH drops under 10.5, ettringite becomes unstable [68]. On the other hand, hydration products of cement were reported to dissolve under a pH of 9 [12]. Therefore, the pH was monitored in this study to investigate the effect of the slag fineness on the ability of the prevention of pyrite mineral oxidation, as well as an indication of the acid buffering capacity. For this purpose, after the UCS tests, the CPBs were grated to under 2.36 mm and placed into a glass beaker. Then, distilled water was poured into the beaker, providing a solid-to-water ratio of 1:1, and mixed thoroughly with a stainless-steel kitchen whisk for 5 min. The mouth of the beaker was covered with a parafilm and stood for one hour. Then, the pH was measured using the clear portion of the solution. Details of the pH and sulphate monitoring method can be found elsewhere [21].

The initial pH and sulphate concentrations of the tailings were 8.98 and 5712 ppm, respectively. The high sulphate concentration was attributed to the sulphate-containing chemicals used and the pyrite oxidations during the ore-processing stages.

2.4. Microstructural Investigation

The microstructural properties of the CPBs produced using slags in three different specific surface areas were investigated in this study, in detail. In this scope, detailed microstructural experimental studies were carried out using a scanning electron microscope equipped with an energy-dispersive X-ray spectroscopy (SEM + EDS) and mercury intrusion porosimeter (MIP). For the microstructural studies, 24 additional CPBs were cast and used at 28-, 112- and 360-day curing times only for these experiments. The obtained results were used to investigate the effect of the slag fineness on the microstructural evolution of the CPBs and the durability properties.

The SEM + EDS studies were conducted at a 15 kV accelerating voltage using a ZEISS-EVO MA-LS Series LEO 1550 SEM device (Carl Zeiss Microscopy GmbH, Jena, Germany). The EDS analyses were performed for the phase definitions and the determination of the Ca/Si ratios at the corresponding curing periods to evaluate the acid and sulphate effects [19]. Detailed procedures for the sample preparation for the SEM studies and Ca/Si determination can be found elsewhere [69].

To investigate the relation between the porosity and pore structure, and the strength and durability properties of the CPBs, porosity tests were carried out using a mercury intrusion porosimeter (MIP) with Micromeritics AutoPore IV Series 9510 MIP device (Micromeritics, Norcross, GA, USA), based on ASTM D4404-18 [70], on the samples at 28, 112, and 360 days of curing time. Details of the procedures for the preparation of the CPBs for the MIP tests can be found elsewhere [69]. The obtained results of the MIP tests were assessed based on the International Union of Pure and Applied Chemistry [71] classification.

2.5. Ultrasonic P-wave Velocity Testing

Ultrasonic P-wave velocity (UPV) tests were performed on the CPBs before the UCS tests using a Portable Ultrasonic Nondestructive Digital Indicating Tester (PUNDIT Plus 6; CNS Farnell Limited, Hertfordshire, UK) according to ASTM C597-22 [72]. The end surfaces of the CPBs were flattened and the lengths of the CPBs were measured with an accuracy of $\pm$0.1 mm. Then, the surfaces were covered with a thin layer of gel to maintain a good contact between the transducers and the CPBs. The transit time between the transducers (transmitter and receiver; 42 mm in diameter with 54 kHz) was measured in the continuous mode. Details of the applied procedures for the UPV testing can be found elsewhere [51]. The UPV values (UPVs) were calculated using the following equation, and the mean UPVs are given in the Results for each curing point.

$$UPV = x/t$$

where UPV is the P-wave velocity (m/s), x is the length between the transducers (m), and t is the travel time (μs).

Correlation tests were also carried out to investigate the relationship between the UCSs and UPVs using predictive analytics software (PASW Statistics 18).

3. Results and Discussion

3.1. Effect of the Slag Fineness on the Strength Evolution and Durability Properties of the CPB

The strength (UCS) evolution of the CPB samples is given in Figure 2a. All the CPBs provided the desired UCS at 28 days. The highest strength was obtained from the AAS-6300 samples at 28 days, while the AAS-3100 samples produced the lowest values. The UCS of OPC increased up to 56 days at a low rate, and tended to decrease afterwards. The loss in strength after 112 days was about 30%, considering the 360-day strength dropping under the level of the 14-day strength. Similar tendencies in the OPCs produced from sulphide-rich tailings were obtained in the long term in the previous studies by Cihangir

et al. [69]. The loss in strength of the OPC-CPBs can be attributed to the high CaO content and the poor gel structure.

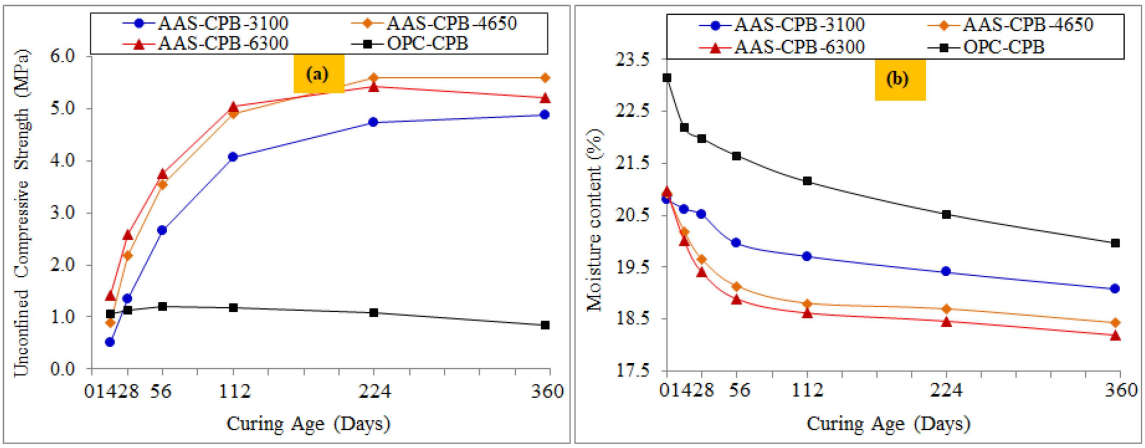

Figure 2. Effect of the slag fineness on the UCS evolution (**a**) and variation in the water/moisture content (**b**) of the CPBs over the curing period.

The AAS-CPBs showed a very high increasing trend and a high slope in the strength gain up to 112 days, and displayed a slower increasing trend afterwards. The 360-day strengths of the AAS-3100, AAS-4650, and AAS-6300 series were 9.8-, 6.33-, and 3.70-fold of the 14-day strength values, respectively. The AAS-3100 samples produced lower strengths than those of the AAS-4650 and AAS-6300 CPBs over the curing period. Considering the average strength values of the AASs over the curing period, the highest belonged to the AAS-6300s. The average strength differences between the AAS-3100, AAS-4650, AAS-6300, and OPC-CPBs were 3.03-, 3.78-, and 3.91-fold, respectively. Similar strength differences when the slag fineness was about 4600 cm^2/g were reached in previous studies performed on the sulphidic tailings CPB prepared with AAS in the long term. On the other hand, the highest strength was obtained in the case of AAS-4650 in the long term. The AAS-CPBs showed relatively much better performance and resistance against aggressive environments than that of the OPC [11,19,69,73], except for the AAS-6300 samples, where only a 3.68% strength loss was observed after 224 days.

The hydration degree of the slag and its strength were reported to increase with an increase in the Blaine fineness [73]. The amount of <3 µm slag fraction was found to provide higher early strength [74]. Additionally, Ref. [75] reached <5 µm of the slag material amount, which significantly affected the hydration, and the 0–20 µm amount was crucial for the early-age (≤7 days) strength development. However, they also found and reported that the amount of slag particles coarser than 20 µm decreased the reactivity of the slag, having less effect on early-age strength gain. In the current study, the <3 µm fine-particle amount of the 6300 slag was ~2.5-fold of the 3100 slag, with a 1.5-fold pozzolanic index value (Table 2). Therefore, the AAS-3100 CPBs produced 1.78- and 2.83-fold lower strengths than those of the AAS-4650 and AAS-6300 CPBs at 14 days. These results suggest that the slag fineness and the amount of fine fractions significantly affected the dissolution rate, the amount of C-S-H gel products, and, therefore, the improvement of the strength-gain properties in the AAS-CPBs.

Figure 2 also displays the moisture content of the CPBs over the curing period. The moisture content was at the lowest levels in the AAS-6300 CPBs compared to those of the others. In other words, the consumption of water seemed to increase with the increase in the fineness of the slag. This can be related to the continuous hydration/hydration-product transformation, etc. Shi et al. [73] stated that the strength of the material may decrease due to the increase in the water demand for the slags whose fineness is over a certain value. Wang et al. [76] also reported that a further increase in the fineness from 5000 to 6000 cm^2/g could cause a decrease in the strength. According to Shi et al. [73], proper strength-development rates may be reached when the fineness of the slag is in the range

from 4000 to 5000 cm^2/g. The findings obtained from this study correspond very well with the related literature mentioned above.

3.2. Effect of the Slag Fineness on the pH and the Sulphate Concentration Evolution of the CPBs

Figure 3 depicts the pH and sulphate concentration levels of the CPBs. The pH values (pHs) of all CPBs displayed an increasing trend up to 14 days. The highest pHs belonged to the OPC-CPBs up to 112 days, which can be attributed to the hydration products, such as C-S-H and $Ca(OH)_2$ (CH:Portlandite) [77]. However, the pHs of the OPC-CPBs tended toward a drastic decline after 112 days, and dropped under a pH of 10.4 at 360 days (Figure 3a), an indication of the continuous oxidation of the pyrite minerals [11,19,69].

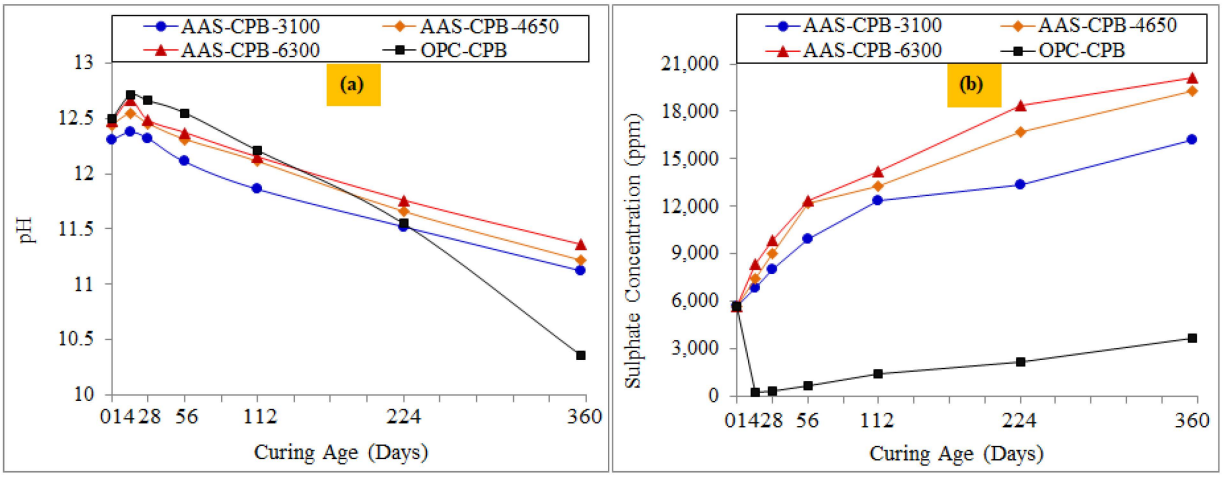

Figure 3. Effect of the slag fineness on the pH (**a**) and the sulphate concentration (**b**) evolution of the CPBs.

As for the AAS-CPBs, the pHs were measured to increase, which can be related to the amount of the higher dissolution rate and the higher formation of hydration products with the increasing fineness of the slag [73,75]. The CPBs with a high slag fineness had high pHs during the curing period. The pHs of all the AAS-CPBs stayed over a pH of 11.10, and the slope of the decreasing trend was relatively very low compared to those of the OPC-CPBs (Figure 3a). Similar results were obtained for the pH levels of the AAS-CPBs in the previous studies [19,21,69]. Additionally, the low early strength of AAS-3100 can be related to the lower pHs slowing down the hydration [78] during the very early ages.

Figure 3b demonstrates the sulphate evolution of the CPBs over the curing period. The OPC-CPBs consumed the initial sulphate ions (Table 1) at an early curing time, which is an indication of sulphate attack. The poor strength-gain rate in the OPC-CPBs at the early ages can be ascribed to the sulphate ion adsorption into the gel products, causing poor-quality C-S-H. Additionally, lower sulphate ion concentrations were an indication of sulphate attack forming expansive reaction products, causing internal stress [73], and the disruption of the OPC-CPBs [21], resulting in strength loss in the long term.

On the other hand, the AAS-CPBs with a higher fineness had higher sulphate ion concentrations over the curing period, as with the pHs. It should also be noted here that the sulphate concentration of the AAS-CPBs reached ~16,000–20,000 ppm, which was thought to stem from the high initial sulphate content of the tailings compared to the authors' previous studies [19,21,69]. As the slag fineness increased, the consumption of sulphate ions seemed to decrease. This can be related to the formation of higher amounts of C-S-H gels with a low Ca/Si ratio, precipitating on the tailings particles in the CPB body. This acts as a protective Si-rich thick layer, decreasing both the rate of pyrite oxidation and the consumption of sulphate ions, as well [21].

3.3. Influence of the Slag Fineness on the Microstructural Evolution of the CPBs

The microstructural properties of the CPBs were examined together with the geochemical studies for both the phase definition and the Ca/Si ratio determination (Figure 4). The gel microstructure in the OPC-CPBs had a fibre-like morphology at early curing ages (Figure 4a,b). Although the microstructure of the OPCs appeared to be dense at the early ages, it became loose as the curing time progressed. One of the reasons stems from the lower solid content of the OPC-CPBs compared to those of the AAS-CPBs (Table 3). Additionally, the morphology tended to turn into a fibre-like/foil-like morphology, which was ascribed to the continuous acid and sulphate effects with the elapse of the curing time (Figure 4c). The bonding of the C-S-H gels was observed to be weak to the tailings' particles. At 28 days, secondary gypsum products were seen to integrate into the C-S-H gels, lowering the product quality, as well. In the SEM examinations performed on the 28-day OPC sample, no obvious crystalline secondary gypsum was encountered, although some small needle-like ettringite crystals were observed to form around the voids (Figure 4a,b). In the long term, obvious secondary gypsum products at different morphologies and coarse needle-like ettringite minerals were observed in the OPC-CPBs (Figure 5). The authors related the loss in strength to the acid and sulphate effects, together with the secondary expansion minerals causing a loose and heterogeneous microstructure [13,14,21,69] .

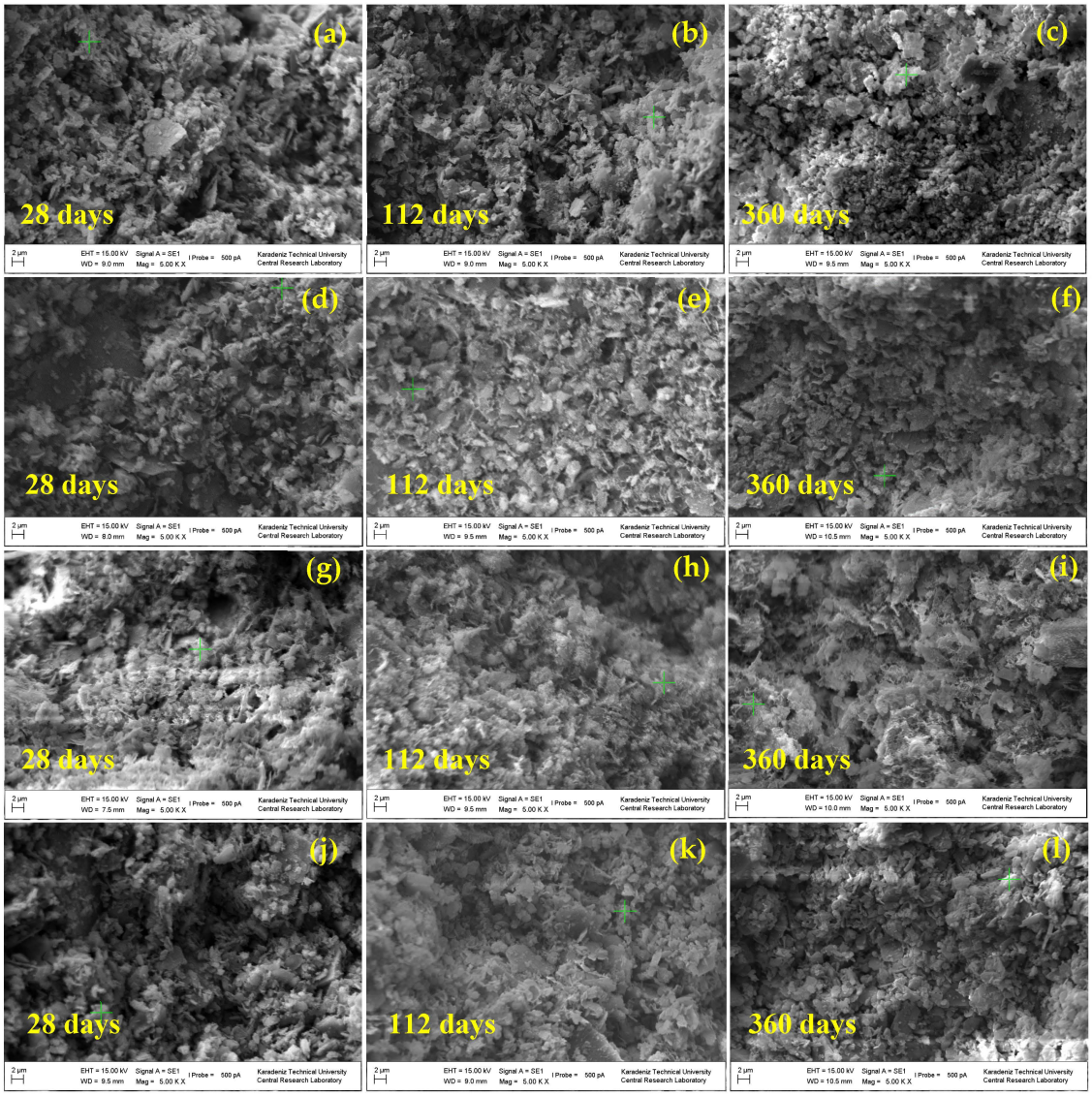

Figure 4. SEM images of the OPC (**a**–**c**), AAS-3100 (**d**–**f**), AAS-4650 (**g**–**i**), and AAS-6300 (**j**–**l**).

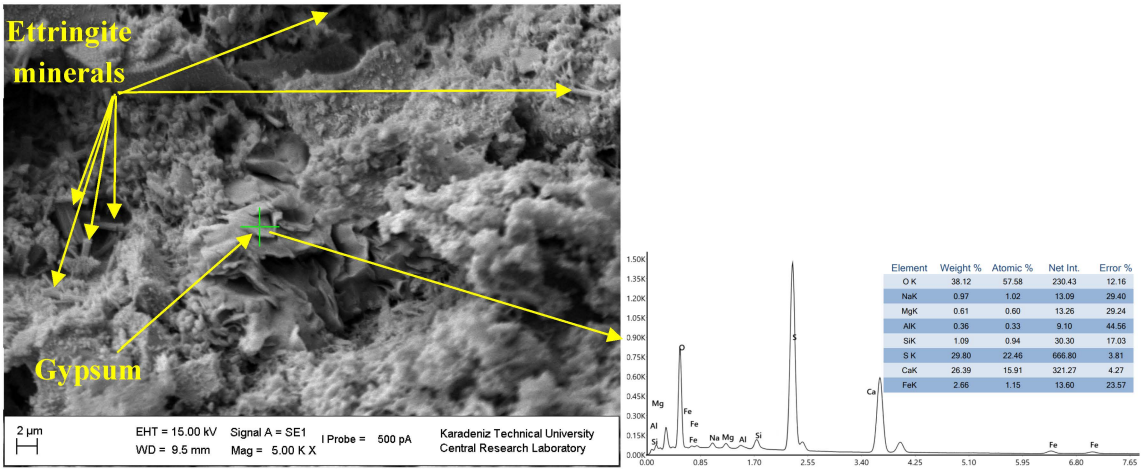

Figure 5. Secondary expansion mineral formations in the OPC-CPB samples and their morphologies.

As for the AASs, all the AAS-CPBs had a foil-like, gel-like (Figure 4d in AAS-3100 and Figure 4l in AAS-6300 samples), and denser microstructure compared to the OPC-CPB. Foil-like hydration products were seen to cover most of the surfaces of the particles and the spaces between particles, which can be related to the continuous strength gain in the AASs. The voids between tailings particles were filled with the newly formed hydration products, with products transformed in other phases and/or other secondary products, such as gypsum, ettringite, monosulphate, etc., with the elapse of the curing time. The microstructure became denser and more compact in all the AASs as the curing time increased. Among the AASs, AAS-4650 had the densest foil-like structure, especially at 112 days and at later ages, while the AAS-6300 sample had a mostly gel-like morphology. The features/morphology of the C-S-H gel products can be seen around the particles and the voids in the AAS-CPBs (Figure 4d–l).

During the SEM examinations and scanning, the amount of secondary mineral phases was found to increase as the fineness of the slag decreased at 112 days and later ages. Very-well-crystallised gypsum minerals, having different morphologies and needle-like ettringites, were observed to form in the air bubbles (Figure 6) and voids as the curing time proceeded to 112 days and thereafter. Secondary gypsum minerals were seen to form especially around and adjacent to pyrite minerals, and the voids between tailings particles in all AASs were the most common and abundant formations encountered in the AAS-3100s during the SEM monitoring (Figures 7, 8 and 9b). Gypsum minerals appeared finer and scattered in/around voids and within the C-S-H gel products in the AAS-6300 sample. Additionally, hexagonal-plate AFm (calcium sulphoaluminates/monosulphoaluminate) phases were seen to be more common in the AAS-6300s (Figure 4l).

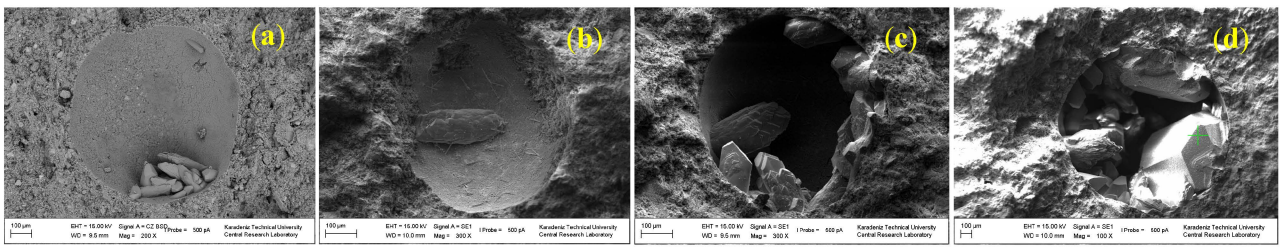

Figure 6. Secondary mineral formations in air bubbles in CPB body: gypsum in AAS-3100 (**a**), gypsum and ettringite in AAS-4650 (**b**), gypsum in AAS-4650 (**c**), and gypsum in AAS-6300 (**d**).

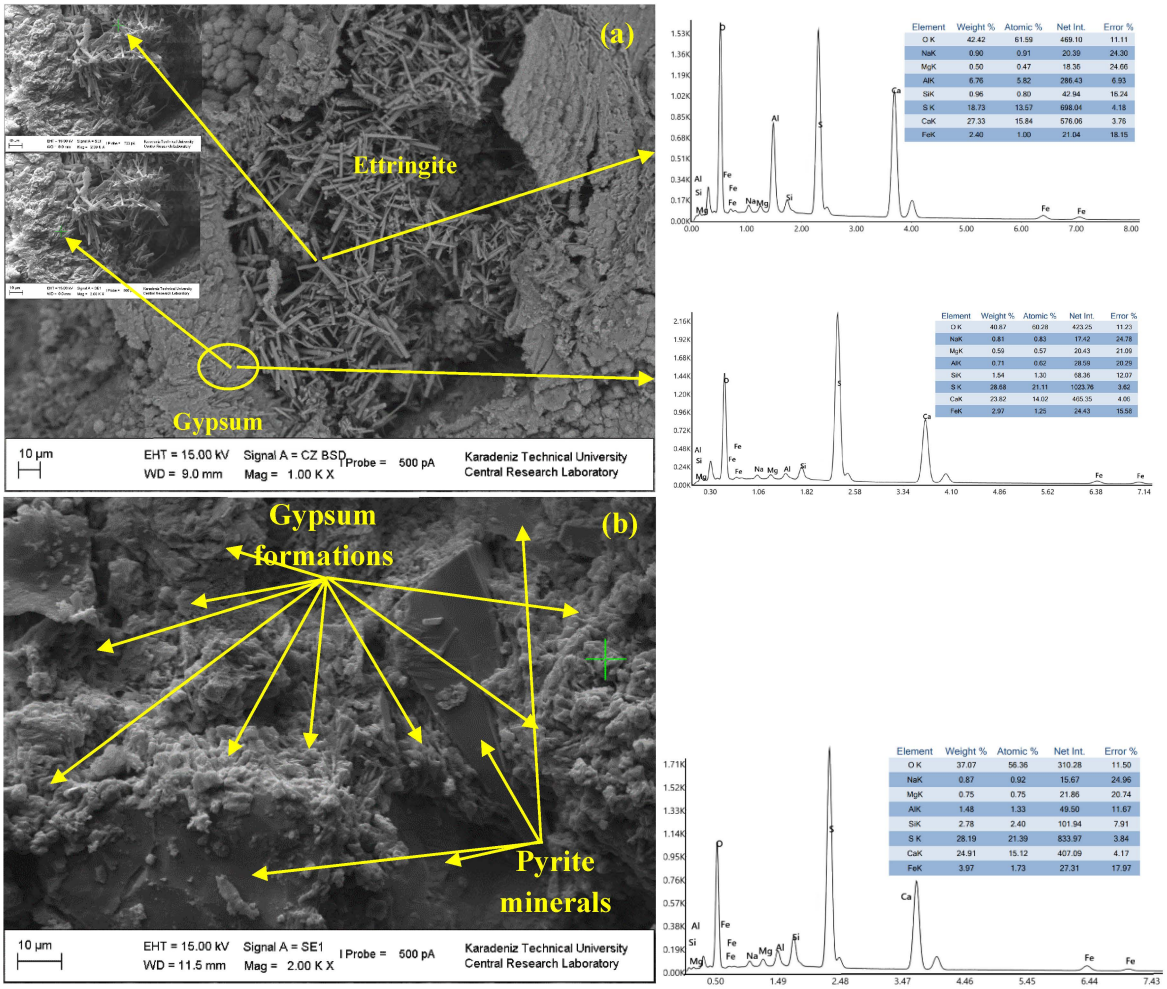

Figure 7. Secondary mineral formations in AAS-3100 at 360 days: ettringite (**a**); gypsum (**b**).

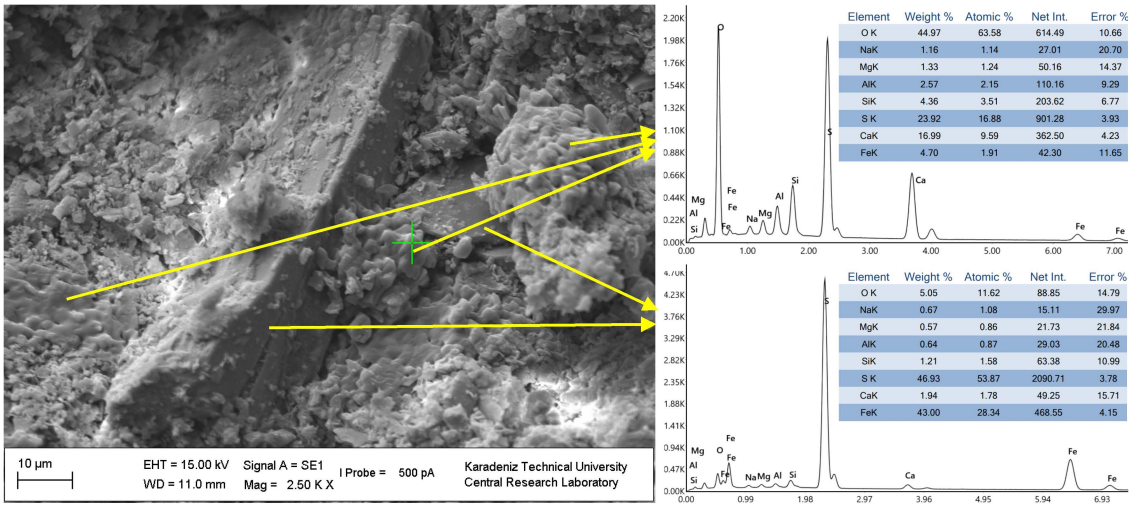

Figure 8. Secondary mineral formations around pyrite minerals in AAS-4650 at 360 days.

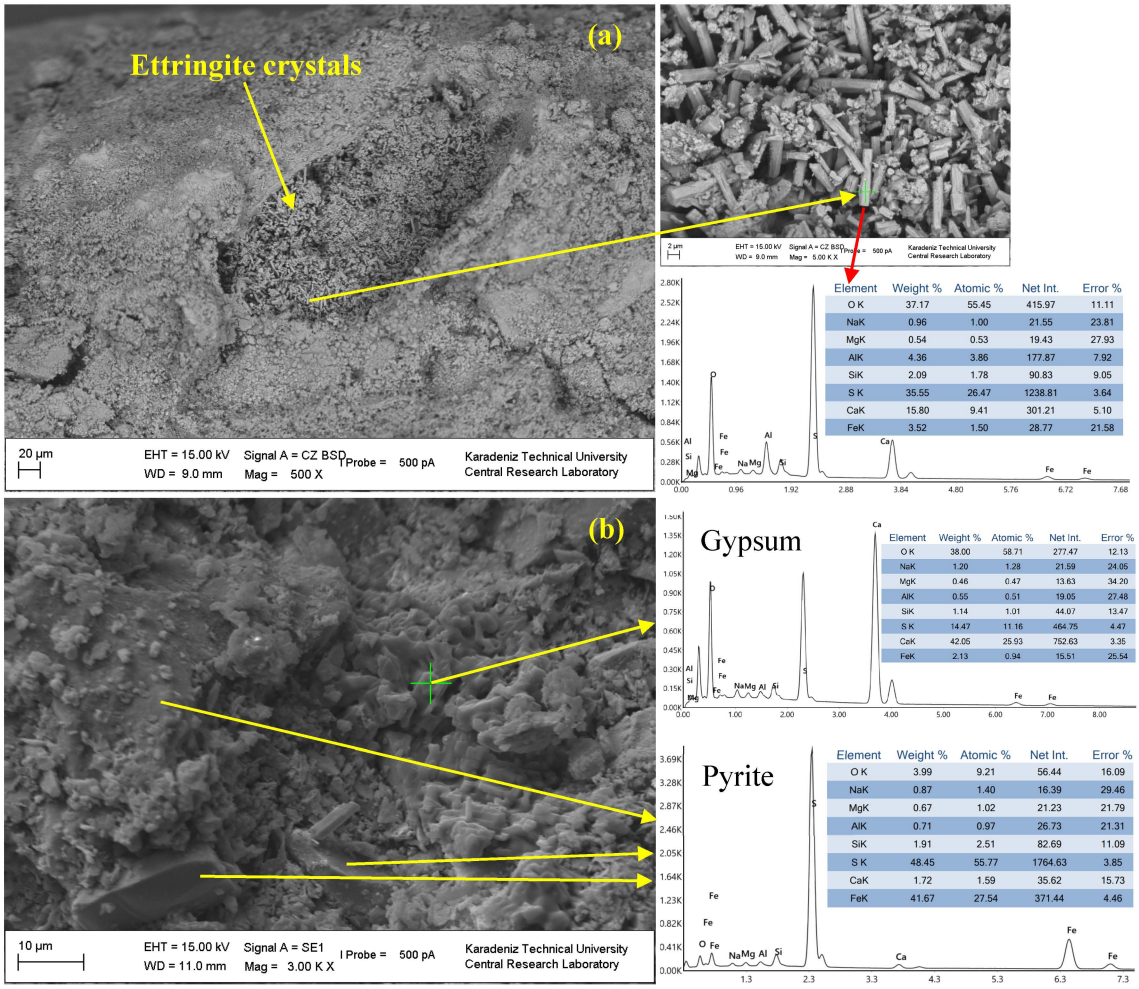

Figure 9. Secondary mineral formations (ettringite (**a**); gypsum (**b**)) in AAS-6300 at 360 days.

It should be noted here that needle-like ettringite minerals were detected within the CPB material for the first time in this study in all the AAS-CPBs. Coarser needle-like ettringites and ettringite clusters were found to form in the air bubbles (Figures 6b, 7a and 9a), similar to the gypsum crystal formations in such bubbles. The authors attribute this phenomenon to the very high initial sulphate ion content compared to the previous studies [11,19,21,69] and the interaction of the tailings with the binder agent [20]. Ettringite was reported to form when Na_2SO_4 was used as an activator and/or sulphates were present in the medium [73].

Some drying shrinkage cracks were observed in the AAS-6300 CPBs after 112 days (Figures 9a and 10). These cracks were thought to result from the decrease in the moisture content in the AAS-6300 samples (Figure 2b). It is well-known that drying shrinkage is caused due to moisture loss. A decrease in strength was reported to occur due to an increase in the water demand with the increasing fineness of the slag. Additionally, drying shrinkage differences between the AAS and OPC samples were reported to increase with the decrease in the relative humidity [73]. Therefore, the decrease in the UCS of the AAS-6300 sample in the long term can be related to such cracks.

Decalcification of the C-S-H products depends on the drop in the pH. With the decrease in the pH, C-S-H releases Ca^{2+} ions for the neutralisation of the acid environment. Therefore, the Ca/Si ratio of the binding-gel products was followed by spot chemical analysis with EDS to monitor the decalcification and assess the durability properties of the CPBs.

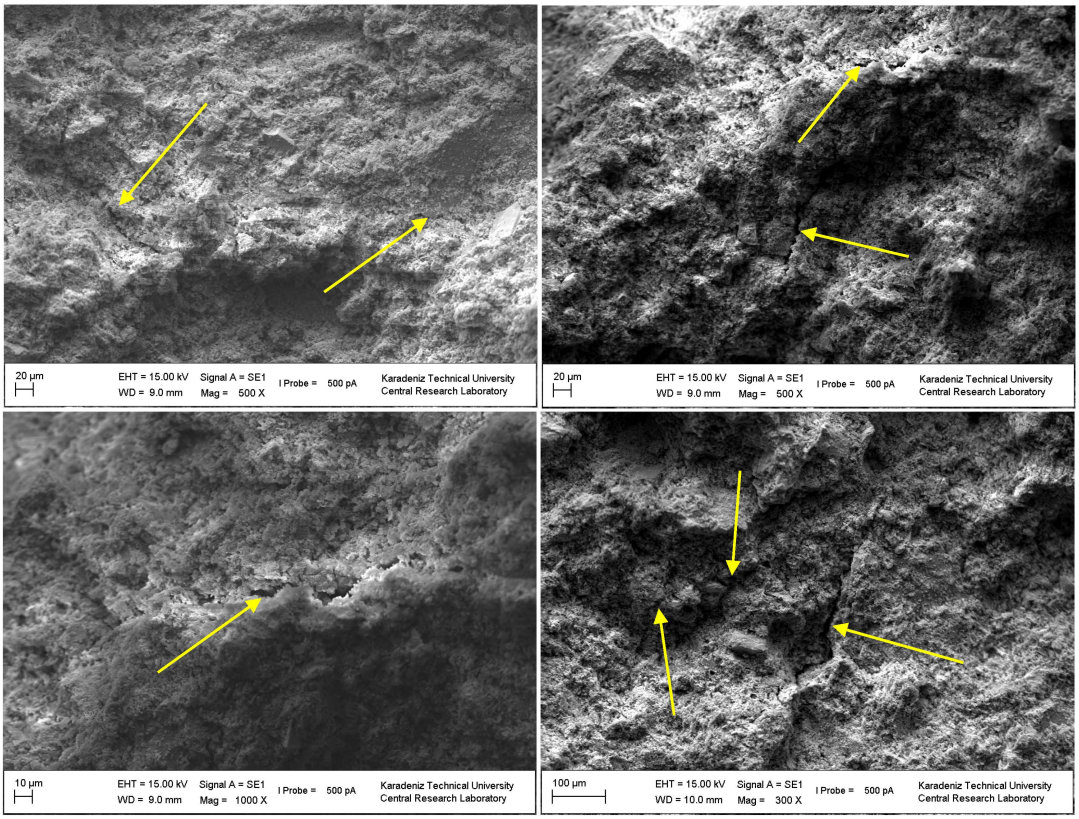

Figure 10. Crack formations in the AAS-6300 CPB after 112 days.

The Ca/Si ratio of the OPCs was 1.90 at 28 days, which dropped to 0.89 at 360 days of curing, an indication of the continuous oxidation of the pyrite minerals. The decreasing trend in the Ca/Si ratio was high at the early stage, which was ascribed to the high initial sulphate content consuming the Ca products (dissolved Ca^{2+} ions, etc.). However, after 112 days of curing, the trend of decrease in the Ca/Si ratio was observed to decline considerably (Figure 11). Although the Ca/Si ratio was 0.89 at 360 days, it appeared to fall even more. The poor strength performance of the OPC-CPBs (Figure 2a) corresponded well with the pH and sulphate ion change (Figure 3), the loose microstructure (Figure 4b,c), and the change in the Ca/Si ratios (Figure 11) with the elapse of the curing time. These findings are in good agreement with the previous studies [19,69]. Decalcification is the most significant phenomenon for the durability performance of cemented materials compared to the expansive phases, such as secondary gypsum, ettringite, etc. [64].

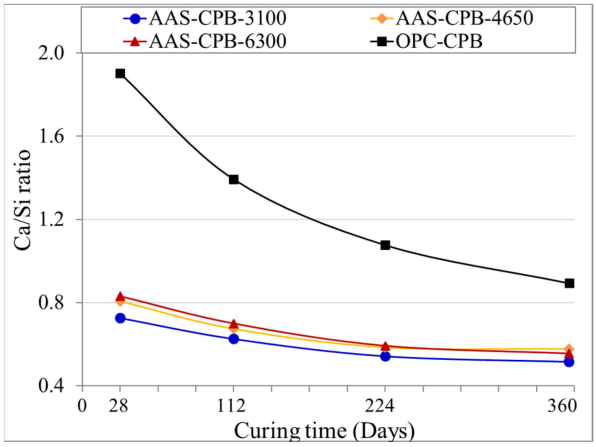

Figure 11. Ca/Si ratio of the binding gels of the CPB samples.

The Ca/Si ratios of the AAS-CPBs were less than those of the OPC-CPBs due to the initially dissolved Si ions coming from the activator and the composition of the slag, of which the Ca/Si ratio was ~0.91. The lowest Ca/Si ratios belonged to the AAS-3100s over the curing period. This can be related to the slower dissolution rate of coarser slag particles releasing fewer Ca^{2+} ions, the consumption of Ca^{2+} ions for the formation of secondary expansive phases, and the dissolved Si ions coming from the activator. The Ca/Si ratios of the AASs were about 0.8 at the early age and 0.55 at 360 days. The trends of decrease were much slighter compared to the OPC-CPBs, where the trends were approximately parallel to the horizontal axis. This can be related to the outer Si-rich protective C-S-H layer covering the surface of the tailings particles, and most importantly, the pyrite minerals reducing oxidation [19,69].

3.4. Pore Size Evolution of the CPB Samples

The pore size distributions (PSDs) and technical parameters of the curves of the CPBs are seen in Figures 12 and 13, respectively. The OPC-CPB sample had the highest total and macroporosities (macropores had a pore size larger than 0.05 µm), and the lowest mesoporosities (mesopores ranged between 0.002 and 0.05 µm) [71,79]. For the given binder dosage, the AASs had a ~38% higher mesoporosity, while the OPC-CPB sample had 18% and 10% higher macro- and total porosities than those of the AASs, respectively. Among the AASs, the 4650 sample had the finest pore structure considering the porosity curves, although total porosity was not the lowest at all curing times (Figures 12 and 13a). At 360 days, the pore size distribution curve of the AAS-6300 sample was seen to swell out/shift to the right, although the total porosity was approximately the same as other AASs (Figure 12b,d,f). Therefore, AAS-6300 had the highest macroporosity at 360 days. This phenomenon can be ascribed to the cracks formed due to internal stress and/or drying shrinkage (Figure 10). This finding very well explains the low decrease in the UCS in the AAS-6300 CPB sample (Figure 2a).

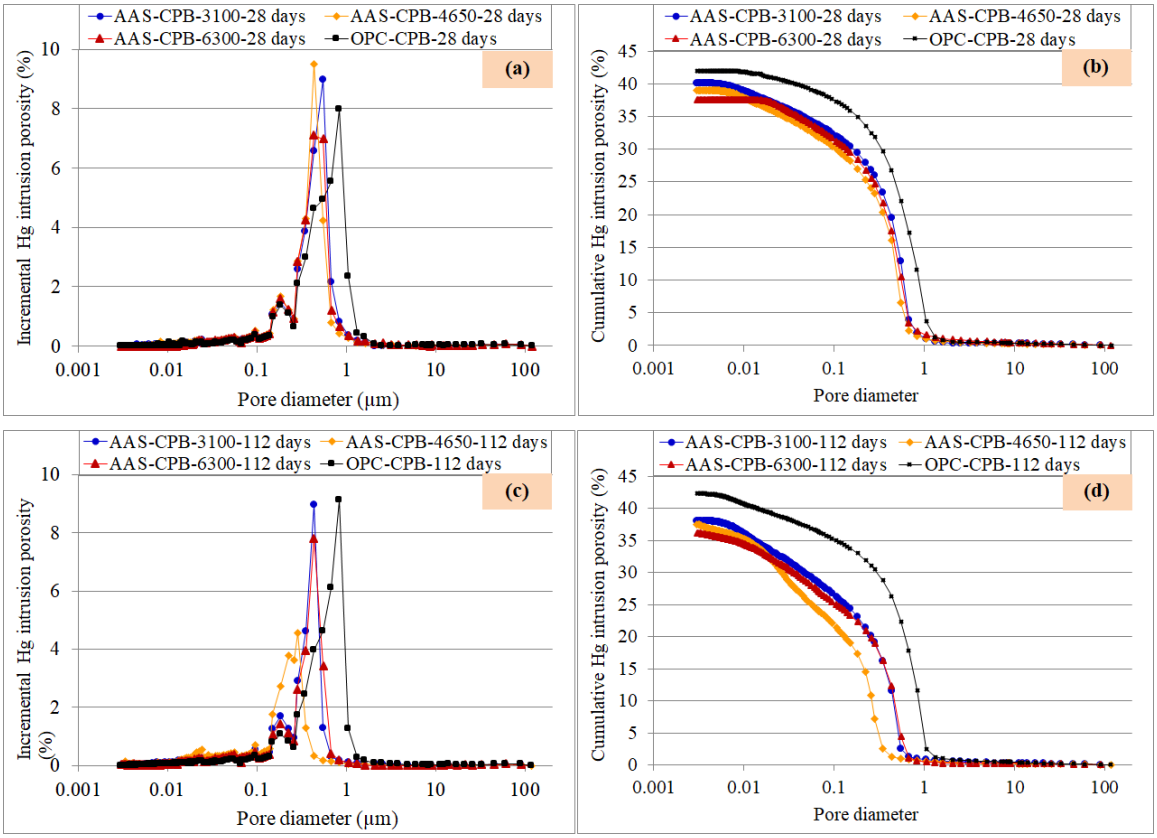

Figure 12. *Cont.*

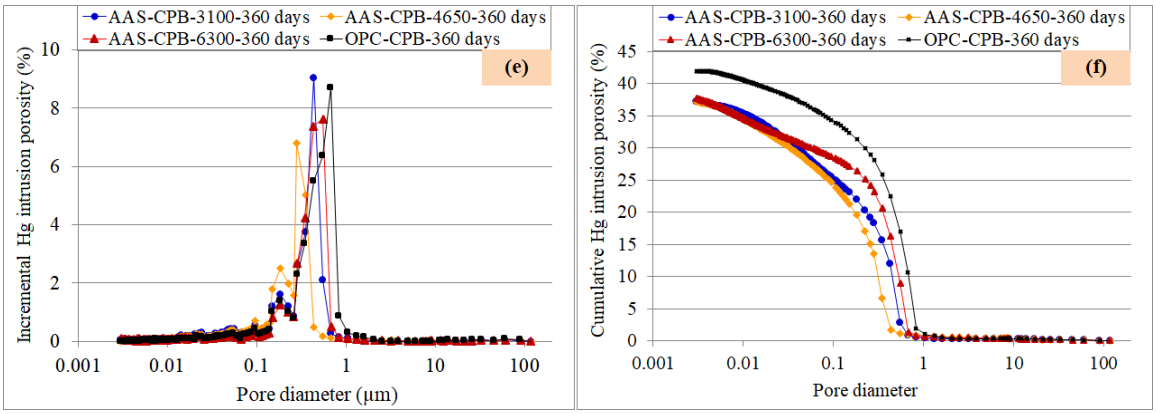

Figure 12. Incremental (**a**,**c**,**e**) and total (**b**,**d**,**f**) pore size distribution curves of the CPB samples.

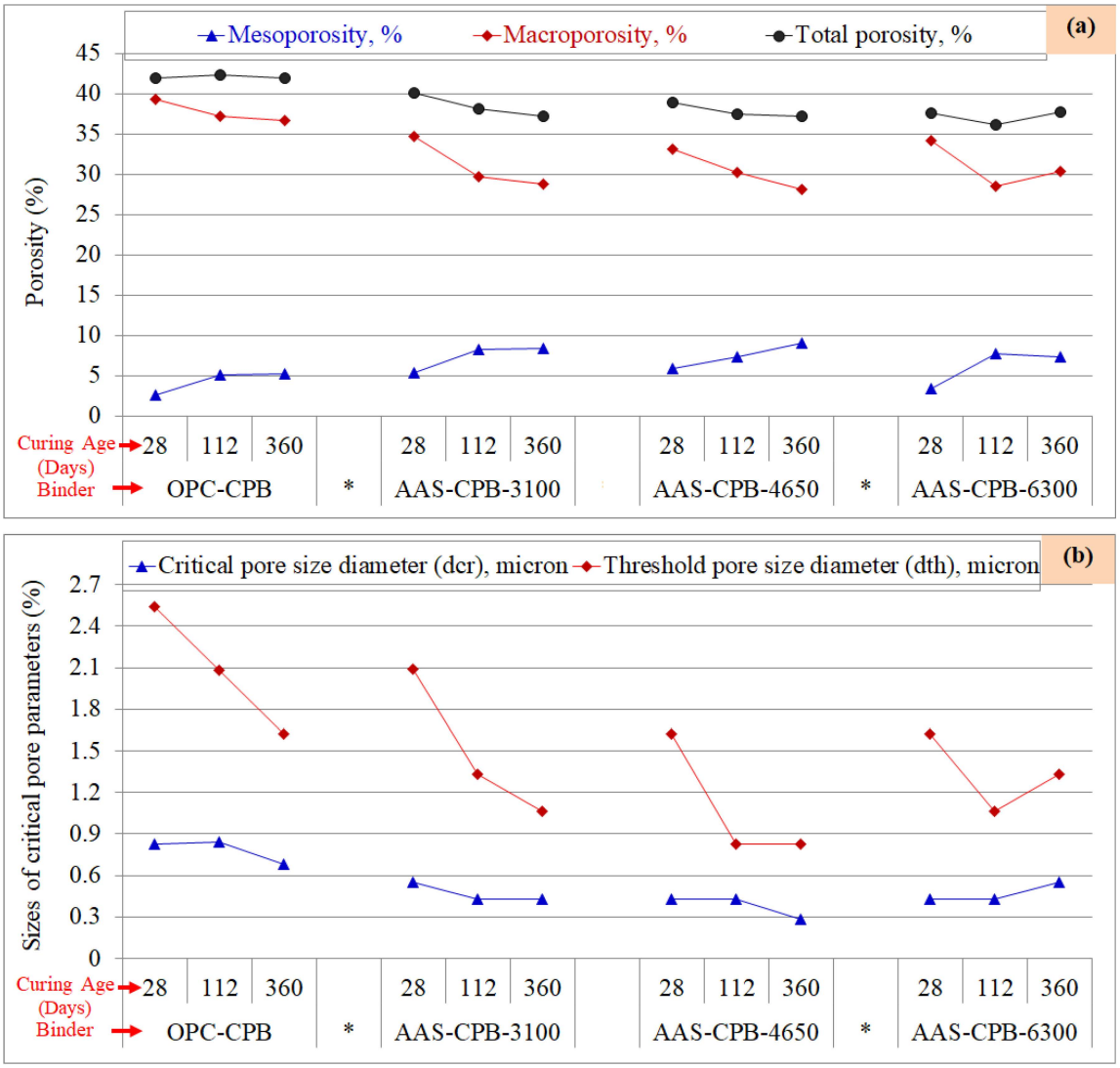

Figure 13. Technical parameters of the pore size distribution curves of the CPB samples: amounts of porosities (**a**), and pore parameters (**b**).

The AAS-CPBs produced lower total porosities than those of the OPC-CPBs in all curing times. The lower total porosities of the AAS-CPBs can be related to the higher solid

contents at the preparation stage, owing to the dispersant and lubricating effects of LSS and the newly formed C-S-H gels [17].

For a given activator, the total porosity and pore sizes were stated to become lower and finer, respectively, when the fineness of the slag increased [73]. In this study, evaluated together with the SEM images, the porous microstructure of the AAS-3100 and AAS-4650 samples were observed to become finer and denser with the progress of the curing time, which was more evident in the AAS-3100 sample. The lower porosity and denser microstructure of these samples can be attributed to the continuous formation of C-S-H, other hydration products, and secondary expansive minerals over the curing period. It seems that the formation of secondary expansive minerals (i.e., gypsum, ettringite) up to a certain amount had a beneficial effect on the decrease in the porosity, improving the compactness (Figure 12) and resistance of the AAS-CPBs against acid and sulphate effects [23,73].

On the other hand, d_{cr}, responsible for fluid transfer in the CPB body, was the highest in OPCs and the lowest in all curing times in the AAS-4650s, as can be seen from Figure 12a,c,e and Figure 13b. As for d_{th} (representing the largest pore diameters), the OPCs had the coarsest pores at all curing times (Figures 12b,d,f and 13b). After 28 days, the d_{th} values were the lowest in the AAS-4650 samples at all relevant curing times, and the highest in the AAS-6300 samples at 360 days among the AAS-CPBs (Figures 12b,d,f and 13b), which is in line with the swelling of the AAS-6300 sample curve towards the right (Figure 12f).

The higher UCS and durability performance of the AAS-CPBs can be related to the quality of the binding gels, the bond strength, the impermeable and protective Si-rich gel products resistant to the aggressive medium and porosity/PSD, etc. [19,64,69,73]. The findings suggest that a further increase in the fineness of the slag does not provide a further advantage in terms of strength, microstructure, and durability.

3.5. Evaluation of the CPB Strength and the Durability Properties via P-Wave Velocity (UPV)

Figure 14a depicts the ultrasonic P-wave velocity (UPV) propagation results of the CPBs. Except for the AAS-3100 and AAS-4650 samples at 14 days, the UPV values (UPVs) of the AAS-CPBs were higher than those of the OPCs at all curing points. Lower UCS values for the AAS-3100 and AAS-4650 samples at 14 days can be ascribed to the slower rate of the strength-development characteristics of the activated slags, and the inhibitory effect of initial high sulphate ion concentration in the CPBs at very early ages [4,19,21,69]. The UPVs of the AASs were 1.15-, 1.22-, and 1.23-fold on average for the AAS-3100, AAS-4650, and AAS-6300 CPBs compared to the OPCs, respectively. Although the AASs produced prominently greater UPVs than those of the OPCs, the differences are very low compared to the UCS values.

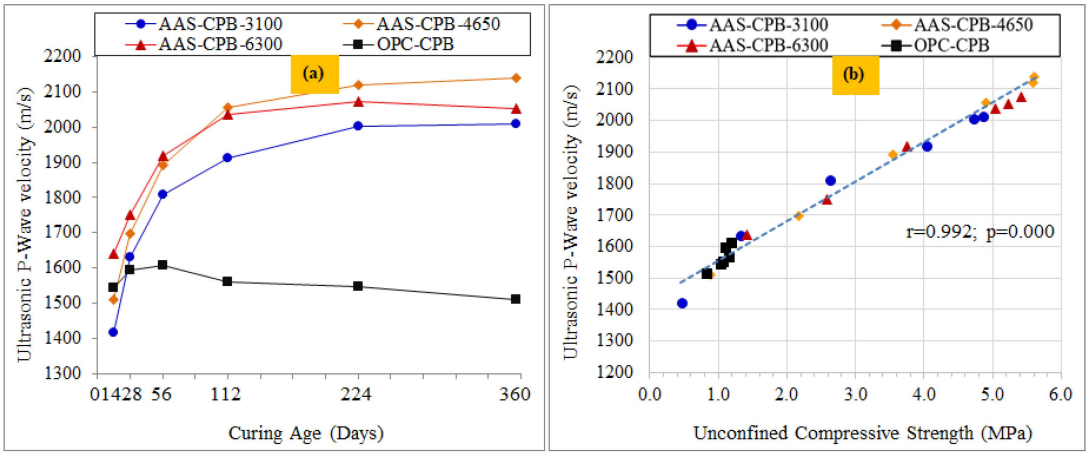

Figure 14. UPVs of CPBs during the curing period (**a**) and the relation between UCS and UPV couples (**b**).

The UPVs of the AASs exhibited a substantial growth trend for the CPBs up to 112 days as a consequence of the intensive formation, densification, and solidification processes of the hydration products, and the slight rate of the rise thereafter. These findings agree well with a similar trend that was obtained between the UPV and UCS couples in previous studies [52]. On the other hand, the UPVs of OPCs displayed a decreasing trend after 56 days, which was parallel to the UCS values. A decrease in the UPV was also seen in the AAS-6300 CPB, as in the UCS, after 224 days. The loss in the UPVs was associated with: (i) acid production, causing decalcification–weathering–loosening in the cemented matrix, and so a reduction in the C-S-H bond strength; (ii) sulphate productions resulting in the disruption–disintegration and the lowering of the material stiffness due to the internal stress, and, so, an increase in the heterogeneity in the OPCs [12,14,21]. Additionally, drying shrinkage cracks (Figure 10) and possible detrimental secondary products were also responsible for the reduction in the UPV of AAS-6300 after 224 days [11,19,66]. Such structural imperfections led to the breakage and diffraction of the UPV waves, resulting in a decrease [80–83].

Higher UPVs for AASs compared to OPCs can be related to the higher solid contents, lower water/cement ratios (Table 3), resistance against acid and sulphate effects (Figure 3), the compact microstructure (Figure 4), the resistance of the binding gels against decalcification (Figure 11), and the lower porosity and finer pore structure (Figures 12 and 13). Higher UPVs can also be attributed to the silicate polymerisation, the higher rate of solidification [73], the quality of the hydration products, and the gain of the strength characteristics of the AAS-CPBs [19,21,69].

There is a similar trend of increase or decrease in the UPVs and UCSs of the CPBs at each corresponding curing point. The coefficient of correlation value between the UCS and UPV couples of the CPBs is very strong, with an "r" value of 0.992 (Figure 11). The direction of the relation is positive, and the relation is significant between each couple within a 95% confidence interval (Table 4). From this point of view, the UPV measurements show that the strength and durability of the CPBs can reliably and simply be followed and/or estimated for a specific CPB design for a mine operation.

Table 4. Relationship between UCS and UPV couples of the CPBs.

Correlation Parameters	Coefficient of Pearson Correlation (r)	Sig. (2-Tailed)
UCS-UPV for all CPB designs	0.992	0.000
UCS-UPV for AAS-3100 CPB samples	0.982	0.001
UCS-UPV for AAS-4650 CPB samples	0.998	0.000
UCS-UPV for AAS-6300 CPB samples	0.997	0.000
UCS-UPV for OPC-CPB samples	0.872	0.023

4. Conclusions

According to the obtained results, AAS provides durable CPBs against acid and sulphate effects when the CPB is made from sulphide-rich tailings. In such a medium, AAS can produce ~four-fold strengths compared to the OPC in the CPB.

The fineness of the slag and fine fraction amounts were found to have an influential effect on the dissolution rate and the amount of hydration-product formation affecting the improvement of the strength-gain properties in the AAS-CPBs, especially in the short term. Hydration-product solidification was observed to slow down with the decreasing fineness of the slag. Further increases in the slag fineness were found to have no advantageous results in terms of the UCS gain. On the contrary, it may have detrimental effects due to the drying shrinkage.

The pH was seen to be high in the case of the increase in the slag fineness. On the other hand, the dissolution rate of the slag particles and the amount of hydration products were found to decrease with the decreasing fineness of the slag. Abundant secondary gypsum, as

well as ettringite minerals, may form in the case of a high sulphate concentration and due to the continuous oxidation of pyrite minerals in the CPB body. Increasing the fineness of the slag was found to unambivalently decrease the secondary expansive mineral formations, but caused drying shrinkage cracks due to the excess moisture loss and/or water demand. The quality of C-S-H is very close in the AAS-CPBs and displays similar resistance against aggressive environments.

The total porosity of the AAS-CPBs decreased with the increasing slag fineness. However, the finest pore structure and the most compact CPBs were reached in the case of the AAS-4650 slag. Secondary mineral formations up to certain amounts were seen to contribute to the decrease in the porosity.

The UPV was very sensitive to the defects and heterogeneity in the CPB body, and was a very effective tool for the evaluation of the durability of the CPB.

Cumulative assessments of the mechanical, geochemical, microstructural, and ultrasonic findings of this study suggest that around a 4600 cm^2/g slag fineness is sufficient for the preparation of the AAS-CPB. Slag in this fineness appears to provide the early-age strength desired for the stability and long-term strength required for the durability of the CPB.

Author Contributions: Conceptualisation, F.C. and E.K.; methodology, F.C. and E.K.; validation, F.C. and E.K.; formal analysis, F.C. and E.K; investigation, F.C. and E.K.; resources, F.C. and E.K; writing—original draft preparation, F.C. and E.K; writing—review and editing, F.C. and E.K; supervision, F.C.; project administration, F.C.; funding acquisition, F.C.; All authors have read and agreed to the published version of the manuscript.

Funding: The authors would like to acknowledge the financial support of The Scientific and Technological Research Institute of Turkiye (TUBİTAK) (project no: 120M534).

Data Availability Statement: All the data that support the findings of this study are available from the corresponding author upon reasonable request.

Acknowledgments: The authors would also like to thank the Askale Cement Trabzon Plant for the analysis support and cement supply, Eti Bakir A.S. for the tailings support, and Karcimsa for the slag supply.

Conflicts of Interest: The authors declare no conflict of interest.

References

1. Chen, Q.; Zhang, Q.; Qi, C.; Fourie, A.; Xiao, C. Recycling Phosphogypsum and Construction Demolition Waste for Cemented Paste Backfill and Its Environmental Impact. *J. Clean. Prod.* **2018**, *186*, 418–429. [CrossRef]
2. Koc, E.; Cihangir, F.; Ercikdi, B. Chapter 3—Geochemical Evaluation of Sulfidic Tailings and Cemented Paste Backfill with Respect to Environmental Impacts. In *Managing Mining and Minerals Processing Wastes Concepts, Design, and Applications*; Qi, C., Benson, C.H., Eds.; Elsevier: Amsterdam, The Netherlands, 2023; pp. 47–70. ISBN 978-0-323-91283-9.
3. Chen, X.; Shi, X.; Zhou, J.; Du, X.; Chen, Q.; Qiu, X. Effect of Overflow Tailings Properties on Cemented Paste Backfill. *J. Environ. Manag.* **2019**, *235*, 133–144. [CrossRef] [PubMed]
4. Meng, J.; Fall, M.; Pour, H.M. Deeper Understanding of the Strength Evolution and Deformation Characteristics of Sodium Silicate–Cemented Paste Tailing Material. *Minerals* **2023**, *13*, 1382. [CrossRef]
5. Petlovanyi, M.; Mamaikin, O. Assessment of an Expediency of Binder Material Mechanical Activation in Cemented Rockfill. *ARPN J. Eng. Appl. Sci.* **2019**, *14*, 3492–3503.
6. Chen, Q.; Zhou, H.; Wang, Y.; Li, X.; Zhang, Q.; Feng, Y.; Qi, C. Resistance Loss in Cemented Paste Backfill Pipelines: Effect of Inlet Velocity, Particle Mass Concentration, and Particle Size. *Materials* **2022**, *15*, 3339. [CrossRef]
7. Wu, D.; Zhao, R.; Xie, C.; Liu, S. Effect of Curing Humidity on Performance of Cemented Paste Backfill. *Int. J. Miner. Metall. Mater.* **2020**, *27*, 1046–1053. [CrossRef]
8. Kasap, T.; Yilmaz, E.; Guner, N.U.; Sari, M. Recycling Dam Tailings as Cemented Mine Backfill: Mechanical and Geotechnical Properties. *Adv. Mater. Sci. Eng.* **2022**, *2022*, 6993068. [CrossRef]
9. Pan, A.; Grabinsky, M. Mechanical Characterization of Cemented Paste Backfill. *Eng* **2023**, *4*, 738–747. [CrossRef]
10. Kesimal, A.; Ercikdi, B.; Yilmaz, E. The Effect of Desliming by Sedimentation on Paste Backfill Performance. *Miner. Eng.* **2003**, *16*, 1009–1011. [CrossRef]
11. Cihangir, F.; Ercikdi, B.; Kesimal, A.; Deveci, H.; Erdemir, F. Paste Backfill of High-Sulphide Mill Tailings Using Alkali-Activated Blast Furnace Slag: Effect of Activator Nature, Concentration and Slag Properties. *Miner. Eng.* **2015**, *83*, 117–127. [CrossRef]
12. Benzaazoua, M.; Quellet, J.; Servant, S.; Newman, P.; Verburg, R. Cementitious Backfill with High Sulfur Content Physical, Chemical, and Mineralogical Characterization. *Cem. Concr. Res.* **1999**, *29*, 719–725. [CrossRef]

13. Fall, M.; Benzaazoua, M. Modeling the Effect of Sulphate on Strength Development of Paste Backfill and Binder Mixture Optimization. *Cem. Concr. Res.* **2005**, *35*, 301–314. [CrossRef]
14. Liu, L.; Xin, J.; Huan, C.; Qi, C.; Zhou, W.; Song, K.I.I.L. Pore and Strength Characteristics of Cemented Paste Backfill Using Sulphide Tailings: Effect of Sulphur Content. *Constr. Build. Mater.* **2020**, *237*, 117452. [CrossRef]
15. Clayton, S.; Grice, T.G.; Boger, D.V. Analysis of the Slump Test for On-Site Yield Stress Measurement of Mineral Suspensions. *Int. J. Miner. Process.* **2003**, *70*, 3–21. [CrossRef]
16. Kesimal, A.; Yilmaz, E.; Ercikdi, B. Evaluation of Paste Backfill Mixtures Consisting of Sulphide-Rich Mill Tailings and Varying Cement Contents. *Cem. Concr. Res.* **2004**, *34*, 1817–1822. [CrossRef]
17. Cihangir, F.; Akyol, Y. Effect of Desliming of Tailings on the Fresh and Hardened Properties of Paste Backfill Made from Alkali-Activated Slag. *Adv. Mater. Sci. Eng.* **2020**, *2020*, 4536257. [CrossRef]
18. Annor, A.; Tarr, K.; Fynn, D. *Mechanical Properties of a Composite Backfill Material*; Core Project on Deep Mining Version: Montreal, QC, Canada, 2006; pp. 128–132.
19. Cihangir, F.; Ercikdi, B.; Kesimal, A.; Ocak, S.; Akyol, Y. Effect of Sodium-Silicate Activated Slag at Different Silicate Modulus on the Strength and Microstructural Properties of Full and Coarse Sulphidic Tailings Paste Backfill. *Constr. Build. Mater.* **2018**, *185*, 555–566. [CrossRef]
20. Benzaazoua, M.; Fall, M.; Belem, T. A Contribution to Understanding the Hardening Process of Cemented Pastefill. *Miner. Eng.* **2004**, *17*, 141–152. [CrossRef]
21. Cihangir, F.; Ercikdi, B.; Kesimal, A.; Turan, A.; Deveci, H. Utilisation of Alkali-Activated Blast Furnace Slag in Paste Backfill of High-Sulphide Mill Tailings: Effect of Binder Type and Dosage. *Miner. Eng.* **2012**, *30*, 33–43. [CrossRef]
22. Ercikdi, B.; Baki, H.; İzki, M. Effect of Desliming of Sulphide-Rich Mill Tailings on the Long-Term Strength of Cemented Paste Backfill. *J. Environ. Manag.* **2013**, *115*, 5–13. [CrossRef]
23. Pokharel, M.; Fall, M. Combined Influence of Sulphate and Temperature on the Saturated Hydraulic Conductivity of Hardened Cemented Paste Backfill. *Cem. Concr. Compos.* **2013**, *38*, 21–28. [CrossRef]
24. Xue, G.; Yilmaz, E.; Song, W.; Cao, S. Compressive Strength Characteristics of Cemented Tailings Backfill with Alkali-Activated Slag. *Appl. Sci.* **2018**, *8*, 1537. [CrossRef]
25. Kou, Y.; Jiang, H.; Ren, L.; Yilmaz, E.; Li, Y. Rheological Properties of Cemented Paste Backfill with Alkali-Activated Slag. *Minerals* **2020**, *10*, 288. [CrossRef]
26. Jiang, H.; Han, J.; Li, Y.; Yilmaz, E.; Sun, Q.; Liu, J. Relationship between Ultrasonic Pulse Velocity and Uniaxial Compressive Strength for Cemented Paste Backfill with Alkali-Activated Slag. *Nondestruct. Test. Eval.* **2020**, *35*, 359–377. [CrossRef]
27. Mohamed, O.A. A Review of Durability and Strength Characteristics of Alkali-Activated Slag Concrete. *Materials* **2019**, *12*, 1198. [CrossRef] [PubMed]
28. Pacheco-Torgal, F.; Castro-Gomes, J.; Jalali, S. Alkali-Activated Binders: A Review. Part 2. About Materials and Binders Manufacture. *Constr. Build. Mater.* **2008**, *22*, 1315–1322. [CrossRef]
29. Sun, Q.; Wei, X.; Li, T.; Zhang, L. Strengthening Behavior of Cemented Paste Backfill Using Alkali-Activated Slag Binders and Bottom Ash Based on the Response Surface Method. *Materials* **2020**, *13*, 855. [CrossRef] [PubMed]
30. Wang, F.; Zhou, M.; Chen, C.; Yuan, Z.; Geng, X.; Yang, S. Solidification of Uranium Tailings Using Alkali-Activated Slag Mixed with Natural Zeolite. *Nucl. Eng. Technol.* **2023**, *55*, 523–529. [CrossRef]
31. Jiang, H.; Qi, Z.; Yilmaz, E.; Han, J.; Qiu, J.; Dong, C. Effectiveness of Alkali-Activated Slag as Alternative Binder on Workability and Early Age Compressive Strength of Cemented Paste Backfills. *Constr. Build. Mater.* **2019**, *218*, 689–700. [CrossRef]
32. Ji, X.; Gu, X.; Wang, Z.; Xu, S.; Jiang, H.; Yilmaz, E. Admixture Effects on the Rheological/Mechanical Behavior and Micro-Structure Evolution of Alkali-Activated Slag Backfills. *Minerals* **2023**, *13*, 30. [CrossRef]
33. Provis, J.L.; van Deventer, J.S.J. *Alkali Activated Materials, State-of-the-Art Report, RILEM TC 224-AAM*; Springer: Dordrecht, The Netherland, 2014; Volume 1, ISBN 978-94-007-7672-2.
34. Kılıç, A.; Teymen, A. Determination of Mechanical Properties of Rocks Using Simple Methods. *Bull. Eng. Geol. Environ.* **2008**, *67*, 237–244. [CrossRef]
35. Altindag, R. Correlation between P-Wave Velocity and Some Mechanical Properties for Sedimentary Rocks. *J. S. Afr. Inst. Min. Metall.* **2012**, *112*, 229–237.
36. Karpuz, C.; Pa¸amehmetog˘lu, A.G. Field Characterisation of Weathered Ankara Andesites. *Eng. Geol.* **1997**, *46*, 1–17. [CrossRef]
37. Hamdi, E.; Lafhaj, Z. Microcracking Based Rock Classification Using Ultrasonic and Porosity Parameters and Multivariate Analysis Methods. *Eng. Geol.* **2013**, *167*, 27–36. [CrossRef]
38. Sousa, L.M.O.; Suárez Del Río, L.M.; Calleja, L.; Ruiz De Argandoña, V.G.; Rey, A.R. Influence of Microfractures and Porosity on the Physico-Mechanical Properties and Weathering of Ornamental Granites. *Eng. Geol.* **2005**, *77*, 153–168. [CrossRef]
39. Ullemeyer, K.; Siegesmund, S.; Rasolofosaon, P.N.J.; Behrmann, J.H. Experimental and Texture-Derived P-Wave Anisotropy of Principal Rocks from the TRANSALP Traverse: An Aid for the Interpretation of Seismic Field Data. *Tectonophysics* **2006**, *414*, 97–116. [CrossRef]
40. Wyering, L.D.; Villeneuve, M.C.; Wallis, I.C.; Siratovich, P.A.; Kennedy, B.M.; Gravley, D.M.; Cant, J.L. Mechanical and Physical Properties of Hydrothermally Altered Rocks, Taupo Volcanic Zone, New Zealand. *J. Volcanol. Geotherm. Res.* **2014**, *288*, 76–93. [CrossRef]

41. Ullah, Z.; Qureshi, M.I.; Ahmad, A.; Khan, S.U.; Javaid, M.F. An Experimental Study on the Mechanical and Durability Properties Assessment of E-Waste Concrete. *J. Build. Eng.* **2021**, *38*, 102177. [CrossRef]
42. El Jazouli, B.; Tsangouri, E. Fire-Exposed Stones in Constructions: Residual Strength, Performance Loss and Damage Mode Shift Due to Mineralogical Transformation and Micro-Cracking. *Eng. Geol.* **2022**, *302*, 106638. [CrossRef]
43. Gupta, A.S.; Rao, S.K. Weathering Indices and Their Applicability for Crystalline Rocks. *Bull. Eng. Geol. Environ.* **2001**, *60*, 201–221. [CrossRef]
44. Wang, P.; Xu, J.; Fang, X.; Wang, P.; Zheng, G.; Wen, M. Ultrasonic Time-Frequency Method to Evaluate the Deterioration Properties of Rock Suffered from Freeze-Thaw Weathering. *Cold Reg. Sci. Technol.* **2017**, *143*, 13–22. [CrossRef]
45. Christaras, B. *P-Wave Velocity and Quality of Building Materials*; WSEAS Press: Cambridge, UK, 2009; pp. 295–300.
46. Wu, J.; Feng, M.; Chen, Z.; Mao, X.; Han, G.; Wang, Y. Particle Size Distribution Effects on the Strength Characteristic of Cemented Paste Backfill. *Minerals* **2018**, *8*, 322. [CrossRef]
47. Yan, B.; Zhu, W.; Hou, C.; Yilmaz, E.; Saadat, M. Characterization of Early Age Behavior of Cemented Paste Backfill through the Magnitude and Frequency Spectrum of Ultrasonic P-Wave. *Constr. Build. Mater.* **2020**, *249*, 118733. [CrossRef]
48. Qiu, J.; Guo, Z.; Yang, L.; Jiang, H.; Zhao, Y. Effect of Tailings Fineness on Flow, Strength, Ultrasonic and Microstructure Characteristics of Cemented Paste Backfill. *Constr. Build. Mater.* **2020**, *263*, 120645. [CrossRef]
49. Wu, D.; Zhang, Y.; Liu, Y. Mechanical Performance and Ultrasonic Properties of Cemented Gangue Backfill with Admixture of Fly Ash. *Ultrasonics* **2016**, *64*, 89–96. [CrossRef] [PubMed]
50. Xu, X.; Sun, X.; Yao, W.; Wu, P.; Qiu, J.; Guo, Z.; Liu, N. Strength and Ultrasonic Characteristics of Cemented Paste Backfill Incorporating Foaming Agent. *Minerals* **2021**, *11*, 681. [CrossRef]
51. Ercikdi, B.; Yılmaz, T.; Külekci, G. Strength and Ultrasonic Properties of Cemented Paste Backfill. *Ultrasonics* **2014**, *54*, 195–204. [CrossRef]
52. Yılmaz, T.; Ercikdi, B.; Karaman, K.; Külekçi, G. Assessment of Strength Properties of Cemented Paste Backfill by Ultrasonic Pulse Velocity Test. *Ultrasonics* **2014**, *54*, 1386–1394. [CrossRef]
53. Yılmaz, T.; Ercikdi, B. Predicting the Uniaxial Compressive Strength of Cemented Paste Backfill from Ultrasonic Pulse Velocity Test. *Nondestruct. Test. Eval.* **2016**, *31*, 247–266. [CrossRef]
54. Xu, S.; Suorineni, F.T.; Li, K.; Li, Y. Evaluation of the Strength and Ultrasonic Properties of Foam-Cemented Paste Backfill. *Int. J. Min. Reclam. Environ.* **2017**, *31*, 544–557. [CrossRef]
55. Jiang, H.; Yi, H.; Yilmaz, E.; Liu, S.; Qiu, J. Ultrasonic Evaluation of Strength Properties of Cemented Paste Backfill: Effects of Mineral Admixture and Curing Temperature. *Ultrasonics* **2020**, *100*, 105983. [CrossRef] [PubMed]
56. Sari, M.; Yilmaz, E.; Kasap, T.; Karasu, S. Exploring the Link between Ultrasonic and Strength Behavior of Cementitious Mine Backfill by Considering Pore Structure. *Constr. Build. Mater.* **2023**, *370*, 130588. [CrossRef]
57. Landriault, D. Backfill in Underground Mining. In *Underground Mining Methods: Engineering Fundamentals and International Case Studies*; SME: Littleton, CO, USA, 2001; pp. 601–614.
58. *TS EN 196-6*; Methods of Testing Cement—Part 6: Determination of Fineness. TSE: Ankara, Turkey, 2020.
59. ISRM. *The Complete Suggested Methods for Rock Characterization, Testing and Monitoring: 1974–2006*; Springer: London, UK, 2007.
60. Bauné, E.; Bonnet, C.; Liu, S. Reconsidering the Basicity of a FCAW Consumable—Part 1: Solidified Slag Composition of a FCAW Consumable as a Basicity Indicator. *Weld. J.* **2000**, *79*, 57–65.
61. *ASTM C989/C989M-22*; Standard Specification for Slag Cement for Use in Concrete and Mortars. ASTM: West Conshohocken, PA, USA, 2022.
62. *ASTM C143/C143M-20*; Standard Test Method for Slump of Hydraulic-Cement Concrete. ASTM: West Conshohocken, PA, USA, 2020.
63. *ASTM C39/C39M-21*; Standard Test Method for Compressive Strength of Cylindrical Concrete Specimens. ASTM: West Conshohocken, PA, USA, 2021.
64. Komljenović, M.; Baščarević, Z.; Marjanović, N.; Nikolić, V. External Sulfate Attack on Alkali-Activated Slag. *Constr. Build. Mater.* **2013**, *49*, 31–39. [CrossRef]
65. Shi, C.; Stegemann, J.A. Acid Corrosion Resistance of Different Cementing Materials. *Cem. Concr. Res.* **2000**, *30*, 803–808. [CrossRef]
66. Gaitero, J.J.; Campillo, I.; Guerrero, A. Reduction of the Calcium Leaching Rate of Cement Paste by Addition of Silica Nanoparticles. *Cem. Concr. Res.* **2008**, *38*, 1112–1118. [CrossRef]
67. Chen, J.J.; Thomas, J.J.; Jennings, H.M. Decalcification Shrinkage of Cement Paste. *Cem. Concr. Res.* **2006**, *36*, 801–809. [CrossRef]
68. Damidot, D.; Glasser, F.P. Thermodynamic Investigation of the CaO Al_2O_3 $CaSO_4$ H_2O System at 25 °C and the Influence of Na_2O. *Cem. Concr. Res.* **1993**, *23*, 221–238. [CrossRef]
69. Cihangir, F.; Akyol, Y. Mechanical, Hydrological and Microstructural Assessment of the Durability of Cemented Paste Backfill Containing Alkali-Activated Slag. *Int. J. Min. Reclam. Environ.* **2018**, *32*, 123–143. [CrossRef]
70. *ASTM D4404-18*; Standard Test Method for Determination of Pore Volume and Pore Volume Distribution of Soil and Rock by Mercury Intrusion Porosimetry. ASTM: West Conshohocken, PA, USA, 2018.
71. Everett, D.H. I Manual of Symbols and Terminology for Physicochemical Quantities and Units, Appendix II: Definitions, Terminology and Symbols in Colloid and Surface Chemistry. *Pure and Applied Chemistry.* **1972**, *1*, 578–593. [CrossRef]
72. *ASTM C597-22*; Standard Test Method for Pulse Velocity Through Concrete. ASTM: West Conshohocken, PA, USA, 2022.

73. Shi, C.; Krivenko, P.V.; Roy, D.M. *Alkali-Activated Cements and Concretes*; Taylor & Francis: London, UK; New York, NY, USA, 2006; ISBN 978-0-415-70004-7.
74. Wan, H.; Shui, Z.; Lin, Z. Analysis of Geometric Characteristics of GGBS Particles and Their Influences on Cement Properties. *Cem. Concr. Res.* **2004**, *34*, 133–137. [CrossRef]
75. Wang, P.Z.; Trettin, R.; Rudert, V. Effect of Fineness and Particle Size Distribution of Granulated Blast-Furnace Slag on the Hydraulic Reactivity in Cement Systems. *Adv. Cem. Res.* **2005**, *17*, 161–167. [CrossRef]
76. Wang, S.-D.; Scrivener, K.L.; Pratt, P.L. Factors Affecting the Strength of Alkali-Activated Slag. *Cem. Concr. Res.* **1994**, *24*, 1033–1043. [CrossRef]
77. Lloyd, R.R.; Provis, J.L.; Van Deventer, J.S.J. Pore Solution Composition and Alkali Diffusion in Inorganic Polymer Cement. *Cem. Concr. Res.* **2010**, *40*, 1386–1392. [CrossRef]
78. Li, Y.; Min, X.; Ke, Y.; Fei, J.; Liu, D.; Tang, C. Immobilization Potential and Immobilization Mechanism of Arsenic in Cemented Paste Backfill. *Miner. Eng.* **2019**, *138*, 101–107. [CrossRef]
79. Yilmaz, E.; Belem, T.; Bussière, B.; Benzaazoua, M. Relationships between Microstructural Properties and Compressive Strength of Consolidated and Unconsolidated Cemented Paste Backfills. *Cem. Concr. Compos.* **2011**, *33*, 702–715. [CrossRef]
80. Gupta, A.S.; Rao, K.S. Index Properties of Weathered Rocks: Inter-Relationships and Applicability. *Bull. Eng. Geol. Environ.* **1998**, *57*, 161–172. [CrossRef]
81. Smolarkiewicz, P.P.; Nogueira, C.L.; Willam, K.J. Ultrasonic Evaluation of Damage in Heterogeneous Concrete Materials. In Proceedings of the European Congress on Computational Methods in Applied Sciences and Engineering. ECCOMAS, Barcelona, Spain, 11–14 September 2000; p. 13.
82. Aydin, E.; Doven, A.G. Influence of Water Content on Ultrasonic Pulse–Echo Measurements Through High Volume Fly Ash Cement Paste—Physicomechanical Characterization. *Res. Nondestruct. Eval.* **2006**, *17*, 177–189. [CrossRef]
83. Vasconcelos, G.; Lourenço, P.B.; Alves, C.A.S.; Pamplona, J. Ultrasonic Evaluation of the Physical and Mechanical Properties of Granites. *Ultrasonics* **2008**, *48*, 453–466. [CrossRef]

Disclaimer/Publisher's Note: The statements, opinions and data contained in all publications are solely those of the individual author(s) and contributor(s) and not of MDPI and/or the editor(s). MDPI and/or the editor(s) disclaim responsibility for any injury to people or property resulting from any ideas, methods, instructions or products referred to in the content.